Journal of Materials Chemistry C

PAPER

View Article Online
View Journal

Cite this: DOI: 10.1039/c7tc05278b

All-atom simulation of molecular orientation in vapor-deposited organic light-emitting diodes†

Yong Youn, ‡[a] Dongsun Yoo, ‡[a] Hochul Song,[a] Youngho Kang, §[a] Kye Yeop Kim,¶[a] Sang Ho Jeon,[b] Youngmi Cho,[b] Kyungchan Chae[b] and Seungwu Han*[a]

Received 18th November 2017,
Accepted 22nd December 2017

DOI: 10.1039/c7tc05278b

rsc.li/materials-c

Molecular orientation in vapor-deposited organic semiconductor films is known to improve the optical and electrical efficiencies of organic light-emitting diodes, but atomistic understanding is still incomplete. In this study, using all-atom simulation of vapor deposition, we theoretically investigate how the molecular orientation depends on various factors such as the substrate temperature, molecular shape, and material composition. The simulation results are in good agreement with experiment, indicating that the all-atom simulation can predict the molecular orientation reliably. From the detailed analysis of the dynamics of molecules, we suggest that the kinetics of molecules near the surface mainly determines the orientation of the deposited film. In addition, the oriented films have higher density and thermal stability than randomly oriented films. We also show that higher mobility of laterally oriented films can be explained in terms of the site-energy correlation.

Introduction

Organic semiconductors have advantages over inorganic semiconductors in cost, flexibility, weight, and efficiency. Owing to these merits, organic semiconductors are currently empowering several high-performing electronic and energy devices, such as organic light-emitting diodes (OLEDs),[1–5] organic photovoltaics,[6–8] and organic thin-film transistors.[9,10] In particular, OLEDs have entered the mainstream market for full-color displays and lighting applications.

Despite successful commercialization, the lifetime, particularly for blue emission, is still a major weakness of OLEDs. This in turn elevated the importance of emission efficiency because it helps lower the power consumption and extend the device lifespan. As such, recently, the fact that the molecular orientation can improve the efficiency of OLEDs is receiving much attention;[11–14] in the past, the molecular orientation in vapor-deposited amorphous films was assumed to be random and isotropic.[11] However, recent studies indicated that rod-like[15–17] or heteroleptic[18] molecules tend to lie parallel to the substrate in vapor-deposited amorphous films. (In the crystalline structure, both horizontal and vertical orientations were reported.[19]) Such horizontal orientations can be beneficial to the device performance. For example, a phosphorescent OLED could exceed the theoretical quantum-efficiency limit of isotropic molecules by preferentially orienting phosphorescent dyes.[12] It was also found that the horizontal orientation improves the out-coupling efficiency[12] and carrier mobility.[20] Furthermore, vapor-deposited films showed exceptional thermal stability comparable to glasses aged over thousands of years,[21–23] implying a prolonged lifetime.

To fully exploit the molecular orientation for improving device efficiency, it is important to understand the atomistic mechanism of the molecular orientation and predict its effect on device properties such as charge transport and thermal stability. There are several factors that are known to correlate with the molecular orientation like the molecular shape,[11] substrate temperature (T_{sub}),[11,22] and material composition in host–dopant systems.[24–26] Explanations at the molecular level were also proposed; in ref. 12, preferred orientation was explained in terms of the supramolecule made of host and dopant molecules. In the case of heteroleptic molecules, it was suggested that the alignment of aliphatic ligands at the vacuum–organic interface leads to the horizontal orientation.[27] However, the full understanding of molecular orientation would ultimately require consideration of the deposition process. In this respect, computer simulation of the deposition process would be a useful vehicle that can fully enlighten the microscopic origin of the

[a] Department of Materials Science and Engineering and Research Institute of Advanced Materials, Seoul National University, Seoul 08826, Korea. E-mail: hansw@snu.ac.kr
[b] Display R&D Center, Samsung Display Co., Ltd, 1 Samsung-ro, Giheung-gu, Yongin-si, Gyeonggi-do 17113, Korea

† Electronic supplementary information (ESI) available. See DOI: 10.1039/c7tc05278b

‡ These authors contributed equally.

§ Present address: Materials Modeling and Characterization Department, Korea Institute of Materials Science, Changwon 51508, Korea.

¶ Present address: LGE Yangjae R&D campus, 38, Baumoe-ro, Seocho-gu, Seoul 06763, Korea.

preferred orientation. Recently, there have been simulations with such motivations,[22,28–30] which examined the effects of T_{sub} and deposition rate on the molecular orientation. They attributed the formation of the orientation to the liquid-like property near the surface. However, ref. 22 and 28 employed coarse-grained or simplified models which lack electrostatic interactions, and also did not examine shape-dependent preferred orientations. The process-dependent film orientation was studied in ref. 29 but the organic molecule in the simulation is rather simple compared to actual molecules in OLEDs. In ref. 30, molecular dynamics simulations of layer-by-layer deposition of TPD molecules were performed and it was found that lateral molecular orientation was preferred, which explained the measured anisotropy in thermal conductivity. However, the influence of substrate temperature on the molecular orientation was not examined.

In this study, using all-atom molecular dynamics simulation of vapor-deposition processes, we theoretically analyze the effects of T_{sub}, molecular shape, and host molecules on the molecular orientation in the deposited film. We show that the simulation results agree well with previous experimental studies, and that our model can reliably predict the process-dependent orientation of actual molecules. We explain in detail the effects of molecular shape and material composition on the molecular orientation. We also assess the thermal stability of the films and analyze the site-energy distribution.

Method

All molecular dynamics simulations are performed by using the LAMMPS code.[31] Organic molecules are described within the all-atom-optimized-potential-for-liquid-simulations (OPLS-AA) force field,[32,33] whose functional form has been widely used in OLED simulations.[34] We used custom-fitted force field parameters for α-NPD and default parameters for other molecules. The detailed information of the force field parameters and their validation is given in the ESI.† To examine the dependence of orientation on the molecular shape, we selected four different molecules as shown in Fig. 1 that are widely used as hole-transport layers in OLEDs:[35–37] 4,4′-bis(N-carbazolyl)-stilbene (BCS), 4,4′-bis(N-carbazolyl)-1,1′-biphenyl (CBP), N,N′-diphenyl-N,N′-bis(1-naphthyl)-1,1′-biphenyl-4,4′-diamine (α-NPD) and 4,4′-bis[(N-carbazole)styryl]-biphenyl (BSB-Cz). These molecules are similar in structure but differ in length and shape, which would help identify the relation between molecular shape and preferred orientation. To be specific, while BCS, CBP, and α-NPD are similar in length, α-NPD is less planar and bulkier than other molecules since naphthyl and phenyl side groups can rotate separately. BCS is slightly longer than CBP, and BSB-Cz is much longer than other molecules. As reference data, the glass-transition temperatures (T_g's) are estimated from melt-quench simulations using 300 molecules and a cooling rate of 0.033 K ps^{-1}. T_g is estimated from the change of thermal expansion coefficients. For the detailed method, we refer to the ESI† (see Fig. S1). The deposition process is simulated in the *NVT* ensemble using a Nosé–Hoover thermostat and a time step

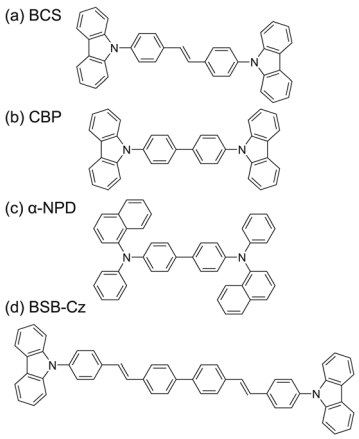

Fig. 1 Organic molecules used in the simulation.

of 1 fs. C_{60} in the face-centered cubic structure is used as a substrate with the surface direction of (100) and the two bottom layers are fixed during the deposition process (see Fig. 2). One may use graphene or Au substrates that are flatter and have stronger interactions with organic molecules than the C_{60} substrate. However, we found that the substrate has little influence on the results except for the interface region (see below) and chose the C_{60} substrate since it is often used in organic electronic devices. To avoid self-interaction caused by periodic boundary conditions, the x and y dimensions of the substrate are set to be longer than three times the molecular length (5.6 nm for BCS, CBP and α-NPD, and 8.4 nm for BSB-Cz).

The deposition simulations are performed at different T_{sub}'s ranging from 300 to 600 K. During the deposition process, a molecule enters the simulation box every 250 ps. This corresponds to the deposition rate of ~1 m s^{-1}, which is much faster than typical experimental conditions (~1 nm s^{-1}). This implies that the present simulation allows much less time for molecular diffusion compared to experiment. To compensate this time-scale gap partly, we accelerate the dynamics of molecules by

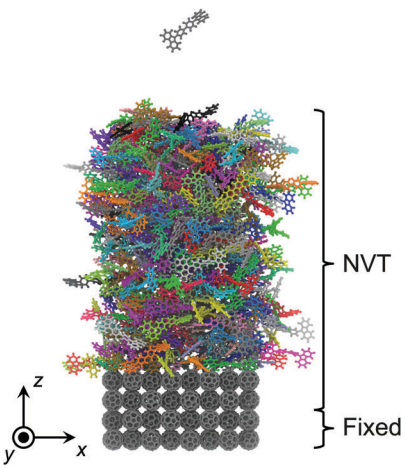

Fig. 2 Snapshot of deposition simulation of CBP molecules. Molecules are colored randomly for visual clarity. The simulation conditions are shown on the right.

maintaining the temperature of the last deposited molecule above the computed T_g. The deposition stops when the film thickness exceeds 10 nm. The molecular orientation with respect to the deposition rate was studied in ref. 28 using a coarse-grained model. It was shown that the faster deposition rate is effectively equivalent to lowering the substrate temperature, which is also confirmed in the present study (see below).

After deposition, the film is allowed to cool down to 300 K at a cooling rate of 0.033 K ps^{-1} and equilibrated for 4 ns. To allow the deposited film to shrink laterally (thermal contraction), the cooling and equilibration simulations are carried out in the *NPT* ensemble. We remove C_{60} layers except two layers during the cooling process. Since the thickness of organic layers ($\sim$12 nm) is 7–8 times larger than that of the C_{60} substrate (1.5 nm), the stress is dominantly affected by organic films rather than the substrate.

The molecular orientation of the film is quantified by the orientational order parameter S that is defined as follows:

$$S = \frac{3\langle \cos^2\theta \rangle - 1}{2} \quad (1)$$

where the angled bracket means the ensemble average, and θ indicates the angle between the direction of the transition dipole moment of the molecule (approximated as the N–N direction along the molecular axis) and the substrate normal. If molecules are perfectly vertical to the substrate, $S = 1$; if every molecule is horizontal to the substrate, $S = -0.5$; for randomly oriented films, $S = 0$. The S value of the deposited film is obtained by averaging over the bulk region, excluding interfacial and surface layers. More than 300 molecules are involved when computing averaged properties of the bulk region (see Fig. S2, ESI† for the z-dependent S factor).

The site energy (E_i^{site}) for holes is evaluated as the sum of the ionization potential (IP) of a gas molecule, conformational energy difference, and electrostatic and polarization energy in a perturbative manner:

$$E_i^{\text{site}} = \text{IP}_{\text{gas}} + \Delta E_i^{\text{conf}} + P_i, \quad (2)$$

where ΔE_i^{conf} and P_i are the conformational energy difference and the electrostatic and polarization energy of molecule i, respectively. The conformational energy difference in eqn (2) is neglected as it is small compared to other terms (see ESI†). The electrostatic and polarization energies are calculated by using AMOEBA polarizable force fields (PFF)[38–40] that are implemented in the TINKER molecular modeling package.[41] The AMOEBA polarizable force field describes both electrostatic interaction and polarization effects. Electrostatic interactions are described by atomic charges, dipoles, and quadrupoles located at the atom center. The polarization effect is described by induced dipoles at each atom center. The dipoles are induced *via* atomic polarizability based on Thole's damped interaction method. For details, refer to ref. 40. PFF parameter sets are obtained as follows: first, charge densities of neutral and charged molecules are evaluated using DFT calculations with NWChem.[42] Then, atom-centered point charges, dipoles, and quadrupoles are computed from the charge densities by distributed multipole analysis.[43] With these parameters, electrostatic and polarization energies are evaluated as

$$P_i = (E^{\text{c}}_{\text{solid}} - E^{\text{n}}_{\text{solid}}) - (E^{\text{c}}_{\text{gas}} - E^{\text{n}}_{\text{gas}}), \quad (3)$$

where E is the total energy with superscripts and subscripts indicating the charge state (c: charged, n: neutral) and the molecular phase, respectively. The energies are evaluated on the structures obtained from the deposition simulations. (The C_{60} substrate is removed.) We employ the Ewald summation to include possible long-range effects originating from molecular orientation. To reduce artefacts from periodically charged excitation, the system is replicated in xy directions, and extended in the z direction to increase the vacuum length. More details of Ewald summation are provided in ESI.† The energies in the gas phase are evaluated within the same periodic system with only molecule i remaining. The model presented in this paper is a microelectrostatic model[44,45] that includes long-range Coulomb interactions. In contrast to the method of Poelking,[46] which describes aperiodic excitation in the periodic background, the present method assumes periodic excitation. To minimize artefacts from this, we extended the system dimension, thereby approximately describing aperiodic excitation. The present approach has a higher computational cost as it calculates interactions that will cancel out eventually, but it has an advantage that it is compatible with most molecular dynamics packages.

Results and discussion

Glass transition temperature

The simulated T_g ($T_{g,sim}$) is listed in Table 1. The available experimental values are also provided for comparison. It is seen that $T_{g,sim}$ is larger than T_g by 100–120 K (see ΔT_g). This is because of much faster cooling rate in the simulation than for actual experiment (0.033 K ps^{-1} *versus* $\sim$1 K min^{-1}). According to the Williams–Landel–Ferry equation,[47] T_g depends on the cooling rate logarithmically, and can increase by up to $\sim$10 K when the cooling rate increases by an order.

Molecular orientation

Fig. 3a shows the S values of the four molecules as a function of T_{sub}. The distribution of S along the z direction indicates that S converges to the bulk value at $\sim$3 nm (6 nm for BSB-Cz) above the interface at which data in Fig. 3a are obtained (see Fig. S2, ESI†). Fig. 3a shows that the characteristic T_{sub}-dependence of the orientation is observed universally, *i.e.*, at low temperatures molecules tend to align laterally while they exhibit random orientation at elevated temperatures. It is also seen that longer

Table 1 Glass transition temperatures of BCS, CBP, α-NPD and BSB-Cz. ΔT_g is the discrepancy between simulated T_g ($T_{g,sim}$) and experimental T_g

Molecule	$T_{g,sim}$ (K)	T_g (K)	ΔT_g (K)
BCS	447	—	—
CBP	459	335[48]	124
α-NPD	473	362[22]	111
BSB-Cz	497	389[20]	108

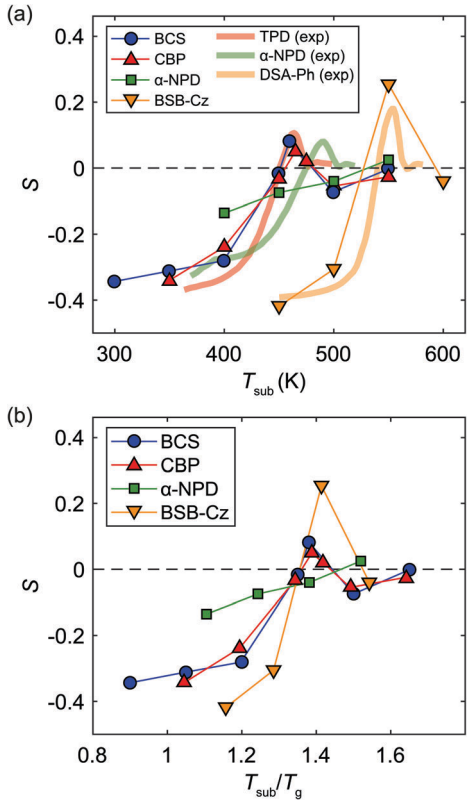

Fig. 3 (a) Orientational order parameter S *vs.* substrate temperature of BCS, CBP, α-NPD, and BSB-Cz. Thick lines indicate experimental values[22] of TPD (blue), α-NPD (green) and DSA-Ph (orange). The experimental data are shifted for the best match with simulation data. (b) Orientational order parameter S *versus* substrate temperature (T_{sub}) normalized by T_g.

or more planar molecules have a stronger tendency to be oriented. For example, BSB-Cz, which is the longest, shows the largest variation in the S value.

In comparison, we also plot in Fig. 3a the experimental data on TPD, NPB, and DSA-Ph from ref. 22 with thick lines. NPB and α-NPD are the same molecule while TPD (DSA-Ph) may well correspond to CBP (BSB-Cz) in terms of the molecular length and shape. The experimental data are shifted for the best match with simulation data. (ΔT = 150, 145, and 210 K for TPD, NPB, and DSA-Ph, respectively.) It is noticeable that the dependence of S on T_{sub} is well reproduced for BSB-Cz and CBP except for rigid temperature shifts. This confirms that increasing the deposition rate is equivalent to decreasing T_{sub} (see above). In particular, small, positive S factors before fully randomized are also reproduced. An explanation on this was given in ref. 22 and will also be discussed below.

In Fig. 3a, the agreement with experiment is rather poor for α-NPD. This is due to more three-dimensional geometry of α-NPD, which hinders surface diffusion of molecules. Since naphthyl and phenyl groups of α-NPD can rotate separately and are out of plane with the long molecular axis, α-NPD molecules are easy to be entangled with each other. (We refer to Fig. 2 in ref. 11 for the three-dimensional conformations of CBP and α-NPD.) The slower diffusion results in rough surfaces because of the fast deposition rate. The rough surface in turn tends to increase the S value, because molecules are deposited on the surface with more upright positions. As a result, the variation of S is rather suppressed for α-NPD in the present simulation. Such effects of rough surfaces also appear at low T_{sub} for other molecules (not shown).

Fig. 3b shows the S values of four target molecules when T_{sub} is normalized by T_g. (For BCS with no extant experiment, we use 333 K by subtracting the average ΔT_g from $T_{g,sim}$.) The universal feature suggested in experiment is also confirmed in the present simulation;[22] in the experiment, the peak is located around T_{sub}/T_g = 0.9 regardless of the molecule type while S peaks at ~1.4 in Fig. 3b. The peak position of T_{sub}/T_g may shift from the experimental value due to the huge gap in the deposition rate.

The comparison with other experiments is also favorable. For instance, S values of α-NPD, CBP, BCS, and BSB-Cz were reported to be −0.01[11] (−0.20[49]), −0.07,[11] −0.17,[11] and −0.33,[11] respectively. The substrate temperatures were not specified in these references but if we sample S values at 420 K (room temperature +120 K), they are estimated to be −0.12, −0.20, −0.25, and −0.42 for the same order of molecules, respectively. Considering experimental and theoretical uncertainties, these agreements are reasonable. Therefore, it is concluded that the all-atom simulation can predict the S values reliably.

In order to understand the atomistic mechanism of preferred orientation, we closely monitored the orientational variation during the deposition and deduced a schematic picture as illustrated in Fig. 4a–d, which is consistent with the mechanism presented in ref. 28. The shaded (green) regions are where molecules can move or rotate freely. At low temperatures, the mobile region is limited to the surface but it gradually expands into the bulk at elevated temperatures (see Fig. S8, ESI†). Fig. 4e shows inherent structure energies and S values in the surface and bulk regions for CBP with respect to T_{sub}. The inherent structure and inherent structure energy are widely used to describe the potential energy landscape of glass.[50] The inherent structure is the one at the local minimum of potential energy (the inherent structure energy). It is obtained by simply relaxing the whole structure at 0 K.

We recall that the surface energy is minimum when molecules are vertically aligned such that the molecular edges are fully exposed to the surface. At low temperatures (Fig. 4a), surface molecules lie horizontally despite higher surface energy (Fig. 4e). This is because deposited molecules cannot rotate due to the thin mobile layer. As the thickness of the surface region increases, surface molecules gradually reorient to reduce the surface energy as in Fig. 4b–d. Consistently, the surface energy in Fig. 4e decreases.

When $T_{sub} < T_g$, molecules barely move in the bulk region. Therefore, the orientation at the surface region dictates the orientation of the film. This accounts for the behavior of S of CBP in Fig. 3a up to 500 K. It also explains a slightly positive value at T_{sub} = 465 K at which a slight vertical alignment at the surface is maintained during deposition. On the other hand, for $T_{sub} > T_g$, molecules are highly mobile in the bulk region and they are randomly oriented as in supercooled liquids (see Fig. 4d).

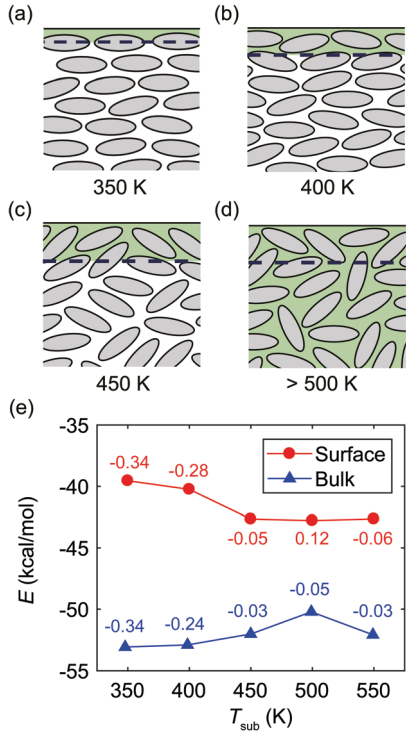

Fig. 4 (a–d) Schematic diagram of CBP films in the vicinity of the surface deposited at (a) 350 K, (b) 400 K, (c) 450 K and (d) 500 K. The green shadows indicate the diffusion region and the area above the dashed line indicates the surface region. (e) The inherent structure energy per molecule of the CBP films relative to the inherent structure energy of a molecule in vacuum. Numbers on the data points are S values of the corresponding region.

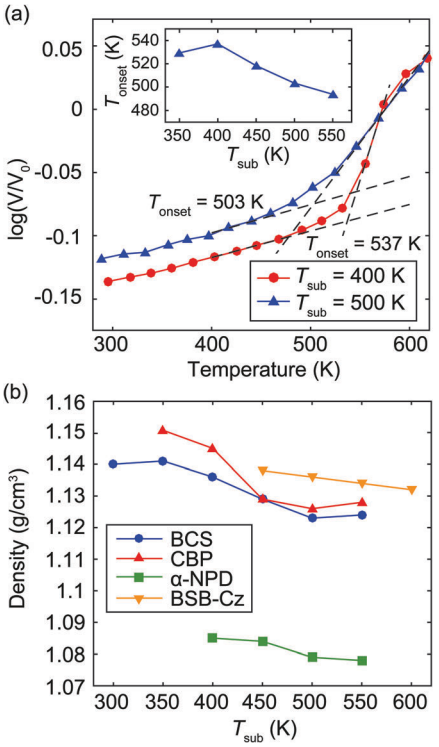

Fig. 5 (a) Change of specific volume during a heating simulation. The inset shows the onset temperature (T_{onset}) of CBP films *vs.* the substrate temperature. (b) The density of the films *vs.* the substrate temperature.

Longer or more planar molecules have higher interaction energies among themselves, and hence stronger propensity to be aligned. That explains why long molecules are oriented more easily. The same argument can be applied to heteroleptic molecules; the heteroleptic molecules at the surface tend to align its aliphatic ligands to reduce its energy.[27] The orientation is frozen as it is buried by other molecules and becomes immobile.

To investigate the influence of substrates on the preferred orientation, we compare the molecular orientation of the film deposited on C_{60} and Au substrates. Due to the strong van der Waals interaction with the substrate, the horizontally oriented interface region is thicker in the Au substrate. However, the order parameter S converges quickly to the bulk value when the film thickness is larger than $\sim$4 nm (see Fig. S9, ESI†).

Thermal stability

The thermal stability of deposited films is an important issue as it is closely related to device lifetime.[51] The thermal stability of the film can be assessed by the onset temperature (T_{onset}) at which the thin film starts to melt. Starting from room temperature, we gradually heat the deposited film with a heating rate of 0.05 K ps^{-1}. In Fig. 5a, the T_{onset} is estimated for CBP films by extrapolating the temperature-dependent volume change (see the dashed lines). It is seen that the laterally oriented films deposited at lower T_{sub} have higher T_{onset}, indicating that the oriented films have higher thermal stability than random structures. The inset shows T_{onset} for various T_{sub}, which agrees well with experiment.[22] This is also consistent with Fig. 4e showing that the bulk energy is lower for molecules deposited at lower temperatures.

Fig. 5b compares the densities of organic films deposited at different T_{sub}. The density is estimated within the bulk part of the deposited film, excluding interfacial and surface regions. It is seen that the density decreases monotonically with T_{sub}, meaning that the oriented films are denser in structure. This is because more compact structures can be obtained by stacking molecules laterally.

In passing, we note that the lateral stacking may not be the unique reason for the higher thermal stability in vapor-deposited films. For instance, isotropic Lennard-Jones particles[52] and metallic alloys[53] also formed vapor-deposited glasses that are far more stable than melt-quenched ones. In these systems, stable glasses were formed because under-coordinated surface molecules could find stable configuration more easily than in the bulk through fast surface diffusion.[54,55]

Host–dopant system

In experiment on host–dopant systems, the orientation of dopant molecules was influenced by host molecules.[24–26] To investigate this, we carry out deposition simulations of the CBP/BSB-Cz mixed system at 450 K. When T_{sub} = 450 K, the CBP film has an S value close to zero, whereas the BSB-Cz film has an S value of –0.4. A set of simulations is performed at the composition ratio of 1 : 9, 2 : 8, 8 : 2, and 9 : 1 (CBP : BSB-Cz). Fig. 6 shows the orientation

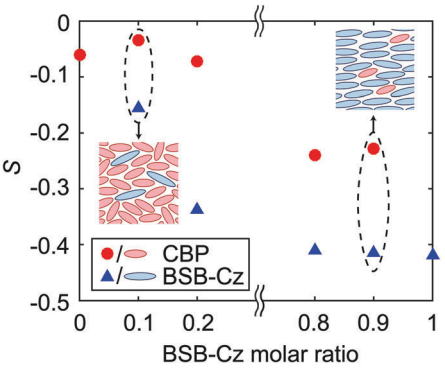

Fig. 6 Orientation order parameter S *vs.* the ratio of BSB-Cz in a CBP/BSB-Cz mixed system. Insets show the schematic configuration of the mixed films of CBP (short and red) and BSB-Cz (long and blue).

of CBP and BSB-Cz molecules with respect to the compositional ratio. It is noticeable that the orientation of dopant molecules becomes closer to that of host molecules. For example, in a CBP dopant/BSB-Cz host system (see the right dashed ellipsoid), CBP molecules are more horizontally oriented than in the pure CBP film, while the orientation of BSB-Cz molecules is not affected by the dopant. Reversely, in the BSB-Cz dopant/CBP host system (see the left dashed ellipsoid), BSB-Cz molecules are more randomly oriented than in the pure BSB-Cz, while the orientation of CBP molecules remained to be random. These observations are because the dynamics of dopant molecules is affected by host molecules. For example, the motions of CBP dopant molecules in BSB-Cz are significantly hindered as BSB-Cz molecules barely move at the temperature as shown in Fig. S10 (ESI†). The simulation results are in good agreement with the previous experimental studies.[24,26]

Site energy distribution

It was reported that the mobility of the horizontally oriented film is more than two times higher than that of the randomly oriented film.[20] The higher mobility of oriented films was attributed to lower energetic disorder and higher transfer integrals.[29] To estimate the influence of molecular orientation on charge transport, we examine the distribution of site energies of CBP films. The site energies are calculated in consideration of the electrostatic and polarization energy of the neighbouring molecules as explained in the Method section. In Fig. 7a, we compare the site energy distributions over the bulk region of the horizontally oriented film and the randomly oriented film. While the mean value is slightly lower for the structure deposited at 550 K, the standard deviation (σ), which is a measure of disorder, is almost the same within the error range. Therefore, the degree of energetic disorder is similar between the two films, which is consistent with ref. 29. Next, we calculate the spatial autocorrelation function $C(r)$ of site energies which expresses the correlation of site energies between two sites at distance r, as defined below:

$$C(r) = \frac{\langle (E-\mu)(E_r-\mu)\rangle}{\sigma^2}, \quad (4)$$

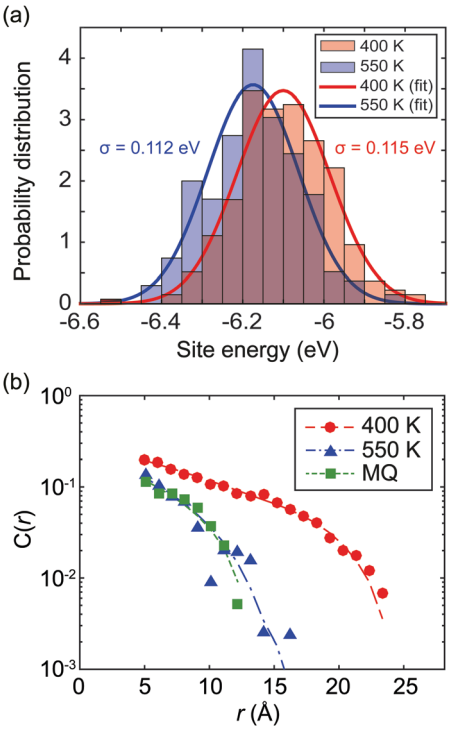

Fig. 7 (a) Site energy distributions, and (b) spatial autocorrelation function ($C(r)$) for the horizontally (T_{sub} = 400 K) or randomly (T_{sub} = 550 K) oriented CBP films. For comparison, $C(r)$ for the melt-quenched CBP film is also presented in (b). Site energy distribution and spatial autocorrelation are evaluated in the bulk region of the film.

where μ and σ are the mean and standard deviation of site energies, and E and E_r are the energies of two sites separated by distance r. The calculated $C(r)$ is shown in Fig. 7b. It is seen that $C(r)$ of the randomly oriented film (T_{sub} = 550 K) is almost the same as that of the melt-quenched sample. However, the horizontally oriented film (T_{sub} = 400 K) shows a higher spatial correlation than the film with random orientation. This means that energy levels of neighbouring hopping sites are similar to each other, which may result in higher mobility. This correlation seems to originate from short-range interactions rather than long-range ones because site energies computed without long-range effects (cluster model) produced similar $C(r)$ (not shown).

Conclusions

In summary, we carried out the all-atom simulation of vapor deposition and investigated how the molecular orientation varies with respect to various factors such as the substrate temperature, molecular shape, and compositional ratio. The simulation results were in good agreement with experiment, confirming many key features in experiment. We showed that the molecular orientation has characteristic dependence on T_{sub}, and molecular shape or host molecules affect the degree of orientation. Through the analysis of inherent structure energy and the kinetic behaviour, we confirmed the mechanism by which the kinetically determined orientation of surface

molecules dictates the *S* factor in the bulk region. The higher thermal stability of oriented films was demonstrated by calculating onset temperatures. The higher spatial correlation in site energies may contribute to the enhanced electrical conductivity of oriented films. In conclusion, we believe that the all-atom simulation is a powerful method to theoretically predict the preferred orientations of amorphous organic films.

Conflicts of interest

There are no conflicts of interest to declare.

Acknowledgements

This research was supported by Samsung Display. The computations were performed at the KISTI supercomputing center (Grant No. KSC-2017-C3-0019).

References

1 M. A. Baldo, S. Lamansky, P. E. Burrows, M. E. Thompson and S. R. Forrest, *Appl. Phys. Lett.*, 1999, **75**, 4–6.
2 S. Reineke, F. Lindner, G. Schwartz, N. Seidler, K. Walzer, B. Lüssem and K. Leo, *Nature*, 2009, **459**, 234–238.
3 B. W. D'Andrade and S. R. Forrest, *Adv. Mater.*, 2004, **16**, 1585–1595.
4 A. P. Kulkarni, C. J. Tonzola, A. Babel and S. A. Jenekhe, *Chem. Mater.*, 2004, **16**, 4556–4573.
5 E. Jung, H. Lee, H. Chae and S. M. Cho, *Electron. Mater. Lett.*, 2015, **11**, 764–768.
6 L. Schmidt-Mende, A. Fechtenkötter, K. Müllen, E. Moons, R. H. Friend and J. D. MacKenzie, *Science*, 2001, **293**, 1119–1122.
7 Y. Sun, G. C. Welch, W. L. Leong, C. J. Takacs, G. C. Bazan and A. J. Heeger, *Nat. Mater.*, 2012, **11**, 44–48.
8 J.-H. Kim, E.-K. Park, J.-H. Kim, H. J. Cho, D.-H. Lee and Y.-S. Kim, *Electron. Mater. Lett.*, 2016, **12**, 383–387.
9 G. Giri, E. Verploegen, S. C. B. Mannsfeld, S. Atahan-Evrenk, D. H. Kim, S. Y. Lee, H. A. Becerril, A. Aspuru-Guzik, M. F. Toney and Z. Bao, *Nature*, 2011, **480**, 504–508.
10 C. Kim, A. Facchetti and T. J. Marks, *Science*, 2007, **318**, 76–80.
11 D. Yokoyama, *J. Mater. Chem.*, 2011, **21**, 19187–19202.
12 K.-H. Kim, S. Lee, C. Moon, S.-Y. Kim, Y. Park, J.-H. Lee, J. W. Lee, J. Huh, Y. You and J. Kim, *Nat. Commun.*, 2014, **5**, 4769.
13 L. Zhao, T. Komino, D. H. Kim, M. H. Sazzad, D. Pitrat, J.-C. Mulatier, C. Andraud, J.-C. Ribierre and C. Adachi, *J. Mater. Chem. C*, 2016, **4**, 11557–11565.
14 D. H. Kim, K. Inada, L. Zhao, T. Komino, N. Matsumoto, J. C. Ribierre and C. Adachi, *J. Mater. Chem. C*, 2017, **5**, 1216–1223.
15 H.-W. Lin, C.-L. Lin, H.-H. Chang, Y.-T. Lin, C.-C. Wu, Y.-M. Chen, R.-T. Chen, Y.-Y. Chien and K.-T. Wong, *J. Appl. Phys.*, 2004, **95**, 881–886.
16 D. Yokoyama, A. Sakaguchi, M. Suzuki and C. Adachi, *Appl. Phys. Lett.*, 2008, **93**, 173302.
17 D. Yokoyama, A. Sakaguchi, M. Suzuki and C. Adachi, *Org. Electron.*, 2009, **10**, 127–137.
18 M. Flämmich, J. Frischeisen, D. S. Setz, D. Michaelis, B. C. Krummacher, T. D. Schmidt, W. Brütting and N. Danz, *Org. Electron.*, 2011, **12**, 1663–1668.
19 H. Yoshida, K. Yamada, J. Tsutsumi and N. Sato, *Phys. Rev. B: Condens. Matter Mater. Phys.*, 2015, **92**, 75145.
20 D. Yokoyama, Y. Setoguchi, A. Sakaguchi, M. Suzuki and C. Adachi, *Adv. Funct. Mater.*, 2010, **20**, 386–391.
21 D. M. Walters, R. Richert and M. D. Ediger, *J. Chem. Phys.*, 2015, **142**, 134504.
22 S. S. Dalal, D. M. Walters, I. Lyubimov, J. J. de Pablo and M. D. Ediger, *Proc. Natl. Acad. Sci. U. S. A.*, 2015, **112**, 4227–4232.
23 K. L. Kearns, S. F. Swallen, M. D. Ediger, T. Wu and L. Yu, *J. Chem. Phys.*, 2007, **127**, 154702.
24 C. Mayr and W. Brütting, *Chem. Mater.*, 2015, **27**, 2759–2762.
25 C.-K. Moon, K.-H. Kim, J. W. Lee and J.-J. Kim, *Chem. Mater.*, 2015, **27**, 2767–2769.
26 J. Jiang, D. M. Walters, D. Zhou and M. D. Ediger, *Soft Matter*, 2016, **12**, 3265–3270.
27 M. J. Jurow, C. Mayr, T. D. Schmidt, T. Lampe, P. I. Djurovich, W. Brütting and M. E. Thompson, *Nat. Mater.*, 2015, **15**, 85–91.
28 I. Lyubimov, L. Antony, D. M. Walters, D. Rodney, M. D. Ediger and J. J. de Pablo, *J. Chem. Phys.*, 2015, **143**, 94502.
29 L. W. Antony, N. E. Jackson, I. Lyubimov, V. Vishwanath, M. D. Ediger and J. J. de Pablo, *ACS Cent. Sci.*, 2017, **3**, 415–424.
30 J. Ràfols-Ribé, R. Dettori, P. Ferrando-Villalba, M. Gonzalez-Silveira, L. Abad, A. Lopeandía, L. Colombo and J. Rodríguez-Viejo, 2017, arXiv:1710.10123.
31 S. Plimpton, *J. Comput. Phys.*, 1995, **117**, 1–19.
32 W. L. Jorgensen, D. S. Maxwell and J. Tirado-Rives, *J. Am. Chem. Soc.*, 1996, **118**, 11225–11236.
33 G. A. Kaminski, R. A. Friesner, J. Tirado-Rives and W. L. Jorgensen, *J. Phys. Chem. B*, 2001, **105**, 6474–6487.
34 F. May, M. Al-Helwi, B. Baumeier, W. Kowalsky, E. Fuchs, C. Lennartz and D. Andrienko, *J. Am. Chem. Soc.*, 2012, **134**, 13818–13822.
35 Z. B. Wang, M. G. Helander, Z. W. Liu, M. T. Greiner, J. Qiu and Z. H. Lu, *Appl. Phys. Lett.*, 2010, **96**, 1–4.
36 M. Sigalov, A. Ben-Asuly, L. Shapiro, A. Ellern and V. Khodorkovsky, *Tetrahedron Lett.*, 2000, **41**, 8573–8576.
37 X. Zhang, Z. Chi, Z. Yang, M. Chen, B. Xu, L. Zhou, C. Wang, Y. Zhang, S. Liu and J. Xu, *Opt. Mater.*, 2009, **32**, 94–98.
38 P. Ren and J. W. Ponder, *J. Comput. Chem.*, 2002, **23**, 1497–1506.
39 P. Ren and J. W. Ponder, *J. Phys. Chem. B*, 2003, **107**, 5933–5947.
40 J. W. Ponder, C. Wu, P. Ren, V. S. Pande, J. D. Chodera, M. J. Schnieders, I. Haque, D. L. Mobley, D. S. Lambrecht, R. A. DiStasio, M. Head-Gordon, G. N. I. Clark, M. E. Johnson and T. Head-Gordon, *J. Phys. Chem. B*, 2010, **114**, 2549–2564.
41 Y. Shi, Z. Xia, J. Zhang, R. Best, C. Wu, J. W. Ponder and P. Ren, *J. Chem. Theory Comput.*, 2013, **9**, 4046–4063.

42 M. Valiev, E. J. Bylaska, N. Govind, K. Kowalski, T. P. Straatsma, H. J. J. Van Dam, D. Wang, J. Nieplocha, E. Apra, T. L. Windus and W. A. de Jong, *Comput. Phys. Commun.*, 2010, **181**, 1477–1489.
43 A. J. Stone, *J. Chem. Theory Comput.*, 2005, **1**, 1128–1132.
44 S. Verlaak and P. Heremans, *Phys. Rev. B: Condens. Matter Mater. Phys.*, 2007, **75**, 115127.
45 S. M. Ryno, S. R. Lee, J. S. Sears, C. Risko and J. L. Brédas, *J. Phys. Chem. C*, 2013, **117**, 13853–13860.
46 C. Poelking and D. Andrienko, *J. Chem. Theory Comput.*, 2016, **12**, 4516–4523.
47 A. Soldera and N. Metatla, *Phys. Rev. E: Stat., Nonlinear, Soft Matter Phys.*, 2006, **74**, 61803.
48 M.-H. Tsai, Y.-H. Hong, C.-H. Chang, H.-C. Su, C.-C. Wu, A. Matoliukstyte, J. Simokaitiene, S. Grigalevicius, J. V. Grazulevicius and C.-P. Hsu, *Adv. Mater.*, 2007, **19**, 862–866.
49 Y. Sakai, M. Shibata and D. Yokoyama, *Appl. Phys. Express*, 2015, **8**, 96601.
50 F. H. Stillinger, *Science*, 1995, **267**, 1935–1939.
51 M. Kim, S. K. Jeon, S.-H. Hwang and J. Y. Lee, *Adv. Mater.*, 2015, **27**, 2515–2520.
52 D. R. Reid, I. Lyubimov, M. D. Ediger and J. J. de Pablo, *Nat. Commun.*, 2016, **7**, 13062.
53 J. Q. Wang, Y. Shen, J. H. Perepezko and M. D. Ediger, *Acta Mater.*, 2016, **104**, 25–32.
54 L. Yu, *Adv. Drug Delivery Rev.*, 2016, **100**, 3–9.
55 S. L. L. M. Ramos, A. K. Chigira and M. Oguni, *J. Phys. Chem. B*, 2015, **119**, 4076–4083.